

## Classification and analysis of common simplifications in part-scale thermal modelling of metal additive manufacturing processes

Ranjan, Rajit; Langelaar, Matthijs; Van Keulen, Fred; Ayas, Can

**DOI**

[10.1186/s40323-023-00253-z](https://doi.org/10.1186/s40323-023-00253-z)

**Publication date**

2023

**Document Version**

Final published version

**Published in**

Advanced Modeling and Simulation in Engineering Sciences

**Citation (APA)**

Ranjan, R., Langelaar, M., Van Keulen, F., & Ayas, C. (2023). Classification and analysis of common simplifications in part-scale thermal modelling of metal additive manufacturing processes. *Advanced Modeling and Simulation in Engineering Sciences*, 10(1), Article 15. <https://doi.org/10.1186/s40323-023-00253-z>

**Important note**

To cite this publication, please use the final published version (if applicable).  
Please check the document version above.

**Copyright**

Other than for strictly personal use, it is not permitted to download, forward or distribute the text or part of it, without the consent of the author(s) and/or copyright holder(s), unless the work is under an open content license such as Creative Commons.

**Takedown policy**


Please contact us and provide details if you believe this document breaches copyrights.  
We will remove access to the work immediately and investigate your claim.

RESEARCH ARTICLE

Open Access



# Classification and analysis of common simplifications in part-scale thermal modelling of metal additive manufacturing processes

Rajit Ranjan<sup>1</sup>, Matthijs Langelaar<sup>1</sup>, Fred Van Keulen<sup>1</sup> and Can Ayas<sup>1\*</sup> 

\*Correspondence:  
c.ayas@tudelft.nl

<sup>1</sup> Delft University of Technology,  
Mekelweg 2, 2628 CD Delft, The  
Netherlands

## Abstract

Computational process modelling of metal additive manufacturing has gained significant research attention in recent past. The cornerstone of many process models is the transient thermal response during the AM process. Since deposition-scale modelling of the thermal conditions in AM is computationally expensive, spatial and temporal simplifications, such as simulating deposition of an entire layer or multiple layers, and extending the laser exposure times, are commonly employed in the literature. Although beneficial in reducing computational costs, the influence of these simplifications on the accuracy of temperature history is reported on a case-by-case basis. In this paper, the simplifications from the existing literature are first classified in a normalised simplification space based on assumptions made in spatial and temporal domains. Subsequently, all types of simplifications are investigated with numerical examples and compared with a high-fidelity reference model. The required numerical discretisation for each simplification is established, leading to a fair comparison of computational times. The holistic approach to the suitability of different modelling simplifications for capturing thermal history provides guidelines for the suitability of simplifications while setting up a thermal AM model.

**Keywords:** Additive manufacturing, Thermal modelling, Simplifications, Laser powder bed fusion

## Introduction

Additive manufacturing (AM), also known as ‘3D printing’, refers to manufacturing techniques in which a three-dimensional part is built by depositing the material layer-by-layer [1]. The key advantage of AM over conventional manufacturing methods (e.g. milling, drilling, casting, etc.) is the form freedom, i.e. geometrically complex parts can be realised without additional process time, cost and assembly [1, 2]. Two sub-classes of AM techniques for building metal parts are powder bed fusion (PBF) and direct energy deposition (DED). Collectively, these techniques are referred to as metal additive manufacturing (MAM). Both use a focused, high-energy beam for locally melting powder particles. The

molten particles fuse and solidify to form a 3D solid shape layer-by-layer. Although these techniques are very similar in process physics, they differ in printing resolution and speed. The layer thickness in the PBF process ranges between 20 and 100  $\mu\text{m}$  while that in the DED process varies between 250  $\mu\text{m}$  to a few millimeters [3,4].

MAM can produce parts with mechanical properties comparable to those produced by conventional manufacturing methods. However, the process still suffers from manufacturing constraints which can cause defects leading to inferior part quality and even complete build failures [5]. For example, design features prone to local overheating adversely affect surface quality. Additionally, during the process, the part undergoes melting/solidification due to severe heating/cooling cycles. This leads to non-uniform thermal expansion and contraction, resulting in deformations and residual stresses [6]. Part geometry and process parameters (such as laser power, scanning pattern, layer thickness, etc.) play an important role in influencing in-process thermal gradients, which subsequently affect residual stress distribution and deformations [7]. Furthermore, the temperature history during the process controls the constituents and morphology of the resulting microstructure, which in turn influences the mechanical properties [8]. Therefore, to ensure consistent MAM part quality, it is crucial to understand the complex relationship between part geometry, process parameters and resulting thermal and mechanical fields. Numerical process modelling of MAM processes is instrumental in achieving this goal. Thermal histories predicted using a numerical model find multiple applications in characterising different aspects of the MAM process. For example, peak temperatures can indicate overheating [9,10]. Consequently, a large number of studies on MAM models exist e.g. [11–13].

It is extremely challenging to model a MAM process, primarily due to two reasons. First, coupling phenomena from various domains of physics are required, e.g., heat transfer, solid mechanics, phase transformation and fluid dynamics [5,14,15]. Second, there is a mismatch of characteristic spatial and temporal scales. For instance, in the laser based PBF process, the laser spot size is approximately 30  $\mu\text{m}$ , whereas the part size is in the order of centimetres. Moreover, in the time domain, melting and re-solidification are extremely rapid because of a fast-moving heat source, whereas the AM process can last up to days for large parts. This multi-scale nature of the process demands a high spatial and temporal resolution to adequately capture the MAM process physics. Consequently, a highly detailed MAM simulation becomes computationally intractable [12]. Therefore, simulations are performed on a very small domain or simplifications are introduced to consider a realistic part size. The former approach, i.e. models at powder or melt pool level [14,16–25] are local models. On the other hand, the latter approach provides a part-scale prediction of temperature, displacement and stress fields, and henceforth is usually called part-scale models [26–35]. This study focusses on the part-scale transient thermal modelling of MAM processes since the thermal response forms the foundation of thermo-mechanical, microstructural and other process simulations. More specifically, we will investigate the implications of thermal modelling choices and simplifications on thermal response predictions.

The common simplifications in the part-scale MAM modelling literature can be mainly classified as simplifications in the spatial and temporal domains. For example, one common simplification in the spatial domain is the simultaneous deposition of an entire layer or a fraction of the layer instead of simulating the laser scanning pattern [36–39]. These simplifications lead to so-called ‘layer-by-layer’ and ‘patch-by-patch’ models, respectively.

Further extension of this idea includes simultaneous deposition of multiple layers, referred to as ‘layer lumping’, ‘superlayers’ or ‘meta-layers’ in the literature. In conjunction with spatial simplifications, assumptions in the temporal domain are also commonly utilised. For example, heating times of 1 ms and 20 ms are considered for each layer in a layer-by-layer simulation by Patil et al. [40] and Zaeh and Branner [27], respectively. Another strategy for defining the heating times of a layer is setting it equal to the total laser processing time of the layer [37,38]. It is noteworthy that the choice for temporal simplification arises as a consequence of introducing the spatial simplifications.

These simplifications provide significant computational benefits at the cost of compromising some degree of accuracy. However, different experimental validation studies have shown that the predictions of such simplified models could be sufficiently accurate to capture specific process characteristics. For example, Chiumenti et al. [37] and Neiva et al. [38] showed that their simplified models could provide accurate predictions of far-field temperatures, i.e. the temperature sufficiently below the topmost layer that is being heated. Bayat et al. [39] showed predictions of a lumped patch-by-patch, thermo-mechanical model can predict deformations of the part with a 90% accuracy. These studies show that it is justified to use certain simplifications to capture specific attributes of the MAM process. However, the scope of the simplifications is discussed on a case-by-case basis in the literature. Generalisation of the validity of a particular simplification for a specific process attribute is absent. Consequently, a fundamental and comprehensive understanding of which simplification is adequate for which purpose is still lacking in the literature. Suitability assessment of different spatial/temporal simplifications for a desired attribute of the thermal history is essential. Therefore in this work, we aim to systematically investigate a range of simplifications and their implications on the accuracy and computational efficiency of thermal simulation predictions. The suitability of different simplifications is assessed and compared with the existing literature to make informed choices while setting up a MAM model.

The outline of the paper is as follows. In “[Classification of simplifications](#)” section, a method for classifying common MAM spatial and temporal simplifications is presented. In “[Model description](#)” section, the governing physics and finite element implementation for MAM process models are described. Based on the novel numerical studies, implications of different simplifications are described in “[Numerical experiments](#)” section. An overview discussion of the insights developed in this study compared to the existing literature is given in “[Discussion](#)” section. Recommendations about simplification choices are presented in “[Recommendations](#)” section. Finally, “[Conclusions](#)” section states the conclusions and future directions.

### **Classification of simplifications**

In this section, a classification scheme is presented for commonly used simplifications in part-scale modelling of the MAM process. Note that this classification scheme is general, and next to thermal modelling, it is applicable to other (e.g. mechanical) MAM simulations. First, the spatial simplifications are further classified based on the material lumping directions. If a simultaneous deposition of material is assumed within the plane of a layer, it is referred to as *in-plane lumping*. A patch-by-patch or a layer-by-layer material deposition assumes various degrees of in-plane lumping. On the other hand, when the thickness

**Table 1** List of the beam spot area  $A_o$ , interaction time  $t_f$  and layer thickness  $l_o$  for EB-PBF, L-BPF and DED processes

Process	$A_o$ (mm <sup>2</sup> )	$t_f$ (ms)	$l_o$ (mm)
EB-PBF [56]	0.007	0.5	0.1
L-PBF [57]	0.007	0.1	0.05
DED [47]	2.009	5.7	0.25

of the material deposition is considered to be an integer multiple of the actual layer thickness, it is referred to as *out-of-plane lumping*. Note that these two types of lumping can also be combined. In the temporal domain, the simplification is characterised by the extension of the heating times  $t_h$ , i.e. how much is the duration of the heating step.

In order to compare the degree of spatial/temporal simplifications across different simplified models from the literature, a normalisation scheme is introduced. For the in-plane lumping, the area of the material  $A$  assumed to be deposited simultaneously, is normalised with the beam spot area  $A_o$ , whereas, for out-of-plane lumping, simulation layer thickness  $l$  is normalised with the actual layer thickness  $l_o$ . In the temporal domain, the normalisation constant is defined as the time laser beam traverses itself, i.e.  $t_f = D/v$ , where  $D$  and  $v$  are beam spot diameter and scanning speed, respectively. Consequently, the normalised in-plane lumping, out-of-plane lumping and heating times are given as

$$\hat{A} = \frac{A}{A_o}, \quad (1)$$

$$\hat{l} = \frac{l}{l_o} \quad \text{and} \quad (2)$$

$$\hat{t}_h = \frac{t_h}{t_f}, \quad (3)$$

respectively. Note that normalisation constants are process dependent and are different for DED and PBF. In PBF, the normalisation constants also differ for the type of high energy beam <sup>1</sup> used to melt the powder. A list of normalisation constants used for each of these processes is given in Table 1.

A 3D simplification space is illustrated in Fig. 1 with axes representing the normalised area deposited  $\hat{A}$ , normalised heating time  $\hat{t}_h$  and normalised layer thickness  $\hat{l}$ . The origin (1, 1, 1) corresponds to simulating the laser movement in real time with actual layer thickness with no simplification. All other points in this simplification space represent a simplified model. The plane of  $\hat{t}_h = 1$  is referred to as the plane of *flash heating models* using the terminology introduced by Bayat et al. [39]. These models have no temporal simplification, while the models above this plane assume extended heating times. Chiu-menti et al. [38], Neiva et al. [37] provide a basis for defining the heating time  $t_h$  for a patch/layer as the time it would take for the beam to process that patch/layer, i.e.

$$t_h = \frac{A}{hv}, \quad (4)$$

where  $A$  is the patch/layer area and  $h$  is the hatch thickness. This type of temporal simplification in this paper is called *gradual heating*. Gradual heating has been used in multiple studies, and it automatically ensures time consistent simulations, i.e. the simulated time

<sup>1</sup> Electron beam based processes are referred to as EB-PBF and laser based processes referred to as L-PBF.

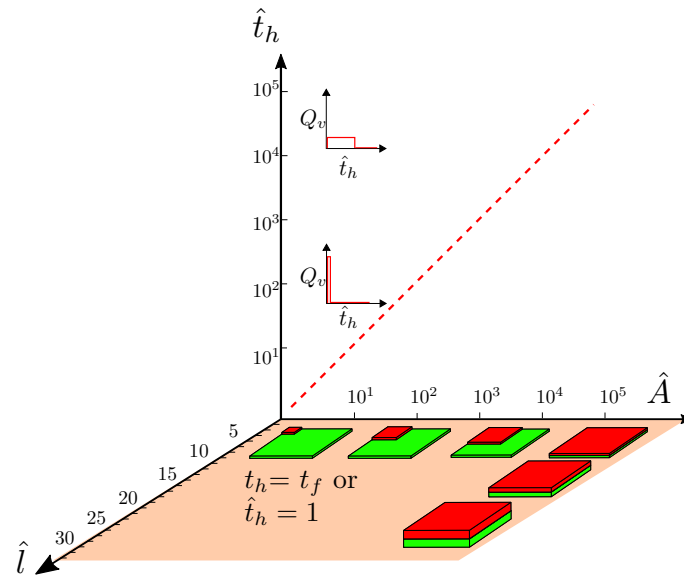


**Fig. 1** A 3D simplification space for quantifying the degree of spatial (in-plane and out-of-plane lumping) and temporal simplifications. The schematic illustrates the spatial simplifications, with the red region indicating the amount of volume assumed simultaneous deposition while the green region indicates previously deposited layer(s). The temporal simplification is represented by extending the heating time while  $\dot{Q}_v'''$  denotes the input power. The dotted red line indicates the gradual heating concept introduced by Chiumenti et al. [37]

is equal to the time elapsed during the AM process. In the literature, it is especially recommended to ensure time consistency for out-of-plane lumping as larger cooling times compensate for the higher heat capacity of thicker lumped layers [36,41]. Any other definition of heating time for a spatially simplified model will require due adjustments in cooling time<sup>2</sup>  $t_c$  to be time consistent. This also implies that gradual heating time presented by Eq. (4) is the upper limit for defining heating time and a value higher than this, will lead to a time inconsistent simulation. The normalised heating time for gradual heating is denoted as  $\hat{t}_g = A/hvt_f$ . A dotted red line is drawn on the  $\hat{A}-\hat{t}_h$  plane in Fig. 1 indicating gradual heating.

**Model description**

L-PBF process is considered here for modelling. The temperatures during the L-PBF process are calculated by numerically solving the heat equation given as

$$\rho c_p \frac{\partial T}{\partial t} = \nabla \cdot (k \nabla T) - \rho \Delta H_{sl} \frac{\partial f_{liq}}{\partial t} + \dot{Q}_v''' \tag{5}$$

where  $\rho$ ,  $c_p$ ,  $k$ ,  $\Delta H_{sl}$ ,  $T$ , and  $t$  are density, specific heat capacity, thermal conductivity, latent heat of fusion, temperature and time, respectively. Thermal conductivity and specific heat capacity are volume-averaged during the solidification interval following

$$k = f_{sol}k_{sol} + f_{liq}k_{liq} \text{ and} \tag{6}$$

$$c_p = f_{sol}c_{p,sol} + f_{liq}c_{p,liq} \tag{7}$$

<sup>2</sup>The time elapsed between two successive layer deposition is referred to as cooling time. The same is also referred to as inter-layer-dwell time or recoater time in the literature.

**Table 2** Thermo-physical properties of Ti6Al4V alloy [39]

$k_{sol}$ and $k_{liq}$ ( $Wm^{-1}K^{-1}$ )	$c_{p,sol}$ and $c_{p,liq}$ ( $Jkg^{-1}K^{-1}$ )	$\Delta H_{sl}$ ( $Jkg^{-1}$ )	$T_{sol}$ (K)	$T_{liq}$ (K)	$\rho$ ( $kgm^{-3}$ )
13, 33	543, 750	286000	1893.2	1927.2	4400

respectively. Here  $f_{sol}$  and  $f_{liq}$  are the solid and liquid fractions, respectively, which sum up to unity and are determined as

$$f_{liq} = \begin{cases} 1 & T \geq T_{liq} \\ \frac{T - T_{sol}}{T_{liq} - T_{sol}} & T_{sol} < T < T_{liq} \\ 0 & T \leq T_{sol} \end{cases}, \quad (8)$$

where  $T_{liq}$  and  $T_{sol}$  are liquidus and solidus temperature of the alloy, respectively. The values for the thermo-physical properties are taken from Bayat et al. [39] and reported in Table 2.

The last term in Eq. (5) is the volumetric heat source  $\dot{Q}_v'''$  due to the laser-material interaction. The following relationship

$$\dot{Q}_v''' t_h = \phi = \frac{\gamma P}{h\nu l_o}, \quad (9)$$

ensures the energy equivalence between all simplified models. Here  $\phi$  is the volumetric energy density,  $\gamma$  is the absorption coefficient and  $P$  is laser power. Note that  $\phi$  remains constant for any spatial or temporal simplification, i.e. over the entire 3D simplification space presented in Fig. 1. Therefore, Eq. (9) provides a basis for calculating the value of volumetric heat source  $\dot{Q}_v'''$  for various simplifications while conserving energy. Based on the above given equations, simulations are performed using finite element analysis in ABAQUS [42] with eight-noded tri-linear C3D8T elements. A Python script is developed for sectioning the part based on the considered spatial simplifications. The element birth and death method is used for sequentially activating the growing domain during AM processes [21,36] using Model change keyword that assumes a linear rise of heat load during the heating step. In order to fully activate the heat load for ensuring energy consistency, a pre-heating dummy step with extremely short period ( $= 10^{-7}$  s) is added in which new material addition is performed. Lastly, the L-PBF normalization constants from Table 1 are used.

### Numerical experiments

In order to study the impact of simplifications on the resulting thermal histories, L-PBF simulation of a simple cuboidal geometry shown in Fig. 2 is considered. A low-volume ( $16 \text{ mm}^3$ ) and geometrically simple part comprising only 20 layers is intentionally considered as it allows to run a high-fidelity simulation located almost at the origin of the simplification space which serves as a reference for other simplified models. Later in “Discussion” section, a brief discussion on usability of simplified models for capturing geometric influence on the thermal history is provided. The part is assumed to be deposited on a base plate, and the dimensions are indicated in Fig. 2. Different levels of simplifications, i.e. different points in the 3D simplification space shown in Fig. 3 are considered. The location of these simplified models in the 3D simplification space is carefully chosen so that the effect

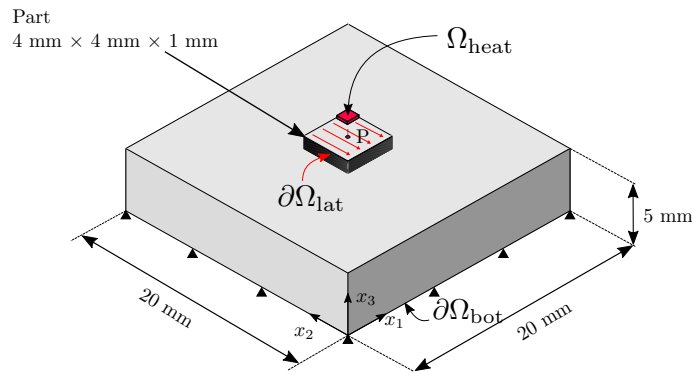


**Fig. 2** Part and baseplate geometry considered for the L-PBF simulation with dimensions. The lateral sides  $\partial\Omega_{lat}$  are assumed to be insulated while a Dirichlet boundary condition is assumed at the bottom of the baseplate  $\partial\Omega_{bot}$ .  $\Omega_{heat}$  represents the region assumed to be deposited simultaneously

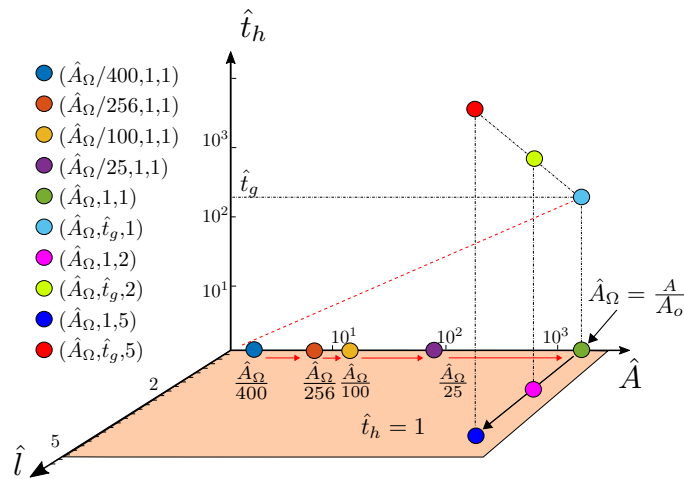


**Fig. 3** Simplified models plotted on the 3D simplification space for analysing the influence of simplifications on thermal history

of each simplification can be systematically studied. The thermal histories obtained with different levels of simplifications are compared to understand the influence of a specific simplification. The center line normal to the plane of the layers is marked in Fig. 2 passing through point P with coordinates (10 mm, 10 mm, 6 mm). Various points on this line, characterised by their  $x_3$  coordinate, are used for comparing the thermal histories across different simplified models marked on Fig. 3.

The bottom face of the base plate is assumed to be maintained at a constant temperature, i.e.  $T = T_0$  on  $\partial\Omega_{bot}$ . The powder conductivity is reported to be approximately 1% of that of bulk material [43, 44]. Hence, the heat conduction through powder is neglected, and thus, the part-powder interface indicated by  $\partial\Omega_{lat}$  in Fig. 2 is assumed to be thermally insulated. The volume of material assumed to be deposited simultaneously is represented as  $\Omega_{heat}$ . The volumetric heat source  $\dot{Q}'''_v$  is defined over the volume  $\Omega_{heat}$ , which varies with the considered spatial simplification. For example,  $\Omega_{heat}$  denotes an entire layer for a layer-by-layer model whereas, for a patch-by-patch model, it represents only a sub-section of the entire layer as illustrated in Fig. 2. Lastly, heat transfer through convection and radiation are considered for the entire topmost part surface with convection coefficient



**Table 3** List of parameters used for thermal modelling of the L-PBF process

$P$ (W)	$\gamma$	$\nu$ (ms <sup>-1</sup> )	$h$ (mm)	$l_o$ (mm)	$t_c$ (s)	$T_0$ (°C)	$T_a$ (°C)	$h_{conv}$ (Wm <sup>-2</sup> K <sup>-1</sup> )	$\epsilon$
120	0.3	0.8	0.08	0.05	4	180	25	10	0.35

$h_{conv}$ , emissivity  $\epsilon$  and ambient temperature  $T_a$ . Material dependent thermal properties for Ti6Al4V are taken from Bayat et al. [39] while relevant process parameters are listed in Table 3.

The simulations are performed for ten different simplified cases as indicated in Fig. 3. The locations of the simplified models are selected such that the effect of each simplification can be isolated. Note that for the cuboid part, all 20 layers have the same area, which, after normalisation, is represented as  $\hat{A}_\Omega$ . The highest fidelity model divides the layer area  $\hat{A}_\Omega$  into 400 equal  $200 \mu\text{m} \times 200 \mu\text{m}$  patches with a thickness of  $50 \mu\text{m}$ . This is represented as  $(\hat{A}_\Omega/400 \approx 5, 1, 1)$  in the simplification space and hereon referred to as the reference model. In a similar manner, coordinates for the remaining nine models are labelled in Fig. 3, which are used for referring to the respective model in the remainder.

### Mesh considerations

In order to determine the numerical spatial and temporal discretisation requirements associated with a particular simplification, a simple numerical experiment is conducted considering 1D heat transfer. The motivation behind using a simplified 1D case is a known analytical solution for a boundary value problem similar to L-PBF. Therefore the simple 1D model has been used to verify the accuracy of different spatial and temporal discretisation schemes. Details associated with the 1D case are presented in “Appendix”, while the primary two findings are examined below.

First, it is found that the definition of heating time  $t_h$  has a direct implication on the required spatial and temporal resolution. This can be explained by appealing to the characteristic length scale  $\kappa = \sqrt{\alpha t_h}$ , [45] indicating the heat affected zone, where  $\alpha$  is thermal diffusivity. For short heating times, i.e.  $\hat{t}_h \approx 1$ , an extremely fine spatial and temporal resolution is required to capture the gradients within this small heat affected zone. As the heating time increases, i.e. temporal simplification approaches the condition of gradual heating  $t_h \approx t_g$ , coarser spatial and temporal discretisation can be used to capture the peak temperatures (see “Appendix”). The required level of discretisation directly affects the computational burden associated with a simplified model. The gradual heating models allowing for a coarser mesh are computationally more advantageous than flash heating models. The computational times associated with different simplified models are reported in “Discussion” section.

Next, far field temperatures away from the heat source during the cooling phase are investigated with the gradual heating scheme. For instance, a material point located a few layers below the topmost layer experiences the heat input with a delay. Consequently, the peak temperature for this point is attained later than that of the topmost layer. It is shown in the study presented in “Appendix” that to capture this delayed peak during the cooling stage, it is important to have a fine temporal resolution, especially at the beginning of the cooling regime.

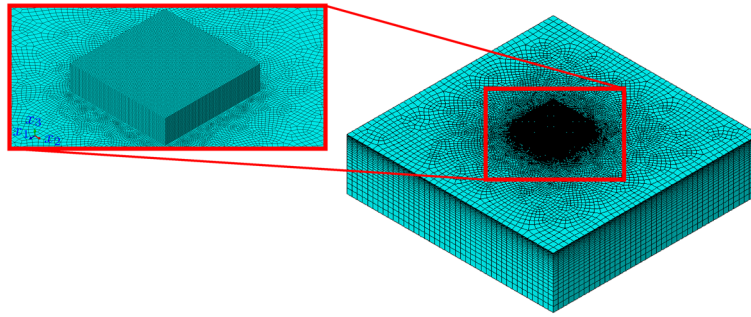


**Fig. 4** Meshing requirements for flash heating. The part is meshed using tetrahedral elements with  $r = 0.05$  mm in accordance with  $\kappa = \sqrt{\alpha t_h}$  considering melting point  $\alpha$  for Ti6Al4V and  $t_h = t_f$  or  $\hat{t}_h = 1$ . The baseplate is meshed with linearly increasing element size from  $r = 0.05$  to  $0.5$  mm, from top to bottom

It remains to apply the findings of the 1D study to mesh the 3D geometry shown in Fig. 2. The part is meshed with tetrahedral linear elements with a mesh size of  $r = 0.05$  mm while the element size for the base plate linearly increases from  $r = 0.05$  mm to  $0.5$  mm, away from the part baseplate interface. The meshed geometry is shown in Fig. 4. This is in accordance with  $\kappa \approx 0.05$  mm for flash heating, assuming a constant  $\alpha$  value taken at the melting point.<sup>3</sup> This meshing scheme is referred to as mesh A and results in approximately 580,000 elements. To check mesh convergence, a more refined discretisation, mesh B is considered with  $r = 0.04$  mm in the part with baseplate elements varying from  $r = 0.04$  to  $0.3$  mm leading to approximately 1,060,000 elements. Deposition of a single patch shown in Fig. 2 is simulated using the reference model characterised by the point  $(\hat{A}_\Omega/400, 1, 1)$  in Fig. 3. The difference between peak and ambient temperatures for the centre point of this patch is compared across both meshing schemes, and it is found to be less than a 1%. This shows that mesh A is sufficient for mesh convergence. Note that  $(\hat{A}_\Omega/400, 1, 1)$  has the most stringent mesh requirements. Therefore the meshing scheme for mesh A ensures the mesh convergence for all the remaining flash heating simulations with a higher degree of spatial simplification. Hence, mesh A is used as the reference discretisation scheme, while coarser meshes are used for gradual heating models in accordance with the relaxed meshing criterion.

#### Influence of in-plane lumping

First, deposition of the initial layer with different patch sizes is considered and obtained thermal histories are compared. These five cases are marked on the axis of in-plane lumping in Fig. 3. The reference model is represented as  $(\hat{A}_\Omega/400, 1, 1)$  where patch-by-patch deposition is assumed in accordance with the scanning directions shown in Fig. 2. The heating time for each patch is equal to the flash heating time  $\hat{t}_h = 1$ , and the heat source intensity is calculated using Eq. (9). The subsequent four models consider larger  $\hat{A}$ , with the largest patch size equal to the entire layer area.

The point at the top of the first layer along the centre line with  $x_3 = 5.05$  mm and labelled by M in Fig. 5 is considered for comparing the thermal histories. This point is chosen since we are first interested in observing the effect of simplifications on the peak temperatures in

<sup>3</sup>Motivation behind using this value of  $\alpha$  comes from findings of Yang et al. [26] that using an  $\alpha$  value at the melting point of the material gives the best thermal predictions upon using temperature independent thermal properties.

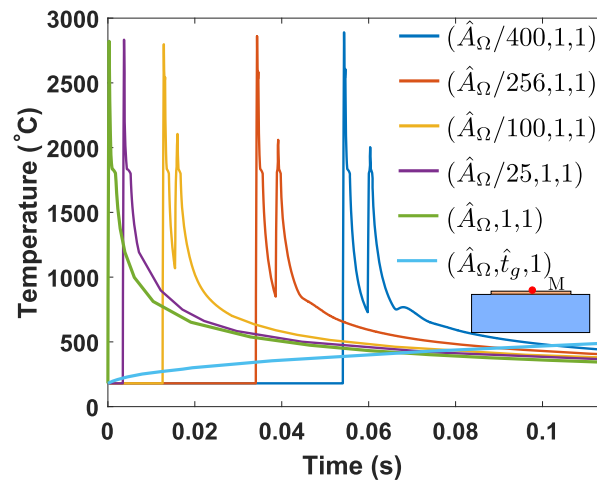


**Fig. 5** Temperature evolution for single layer deposition using simplified models shown in Fig. 3. The temperatures at point M located at (10,5,05,10) in Fig. 2 are plotted with respect to time. Multiple peaks in the thermal history signify the influence of laser scanning, which is not captured by a layer-by-layer simulation. Nevertheless, the variation in the peak temperatures across the range of cases considered is only 3.6%

the vicinity of the heat source. A typical thermal history obtained using a patch-by-patch deposition manifest multiple peaks. The first peak represents the deposition of the patch, which contains the point M and hence the highest temperature peak. The subsequent peaks occur when subsequent neighbouring patches are activated. The thermal history for the case  $(\hat{A}_\Omega, 1, 1)$  exhibits only one peak. The effect of scanning patterns is lost since the entire layer is simultaneously deposited. However, note that the peak temperatures predicted by these models are in close agreement with the highest difference of 2.4% between peak and ambient temperatures across all models. This suggests a layer-by-layer model can provide reasonably accurate predictions for peak temperatures. For example, Ranjan et al. [10], Hodge et al. [9] used peak temperatures calculated as explained above as an indicator of the overheating risk.

Next, we investigate the effects of in-plane lumping with flash heating on far-field temperatures, i.e. the variation of temperature at a point located notably below the heat source. As discussed in “Introduction” section, the far-field temperature history is relevant for predicting microstructure evolution [46]. Moreover, it finds applications for calibrating thermal models against the experimental data obtained using thermocouples typically located a few layers below the topmost layer [37, 38, 47]. For that purpose, points D1 and D2 located on the centre line in Fig. 2 at  $x_3 = 4.75$  mm and  $x_3 = 4.5$  mm, respectively, are considered. This means both D1 and D2 are located in the baseplate five and ten layers below, respectively. The temperature evolution for points D1 and D2 are plotted in Fig. 6. It can be seen that the peak temperatures for the points located away from the heat source are attained after the deposition of the topmost layer is complete. This is demonstrated in the case of  $(\hat{A}_\Omega/400, 1, 1)$  where the end of the heating regime is marked with a dotted vertical line in Fig. 6. Next, a significant influence of laser scanning is observed for patch-by-patch models with small patch sizes. For example, pronounced fluctuations in the thermal history are observed for  $(\hat{A}_\Omega/400, 1, 1)$  in Fig. 6a for point D1 whereas at point D2 a relatively smooth temperature evolution is depicted in Fig. 6b. This demonstrates the influence of scanning strategies is lost after a critical depth.

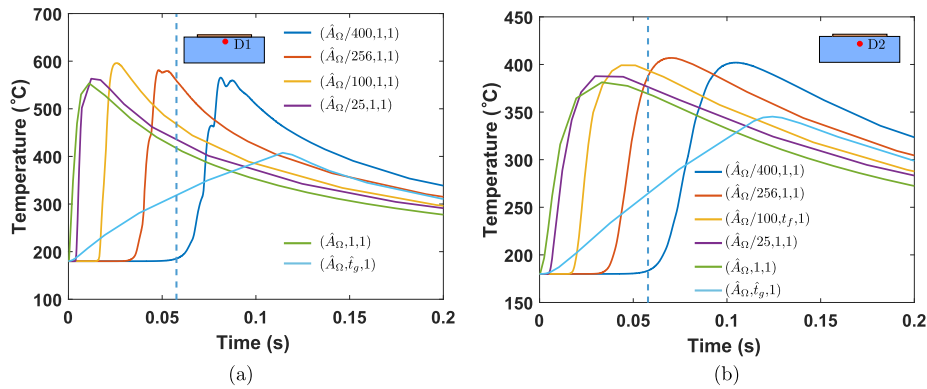


**Fig. 6** Comparison of temperature evolution for simulation of single layer deposition using different levels of fidelity. The variation is shown for points **a** D1 located at 5 layers below and **b** D2 located at 10 layers below in the baseplate

**Influence of heating time**

Next, we investigate the influence of extending heating times on thermal evolution. We first compare flash heating results presented in previous section with a layer-by-layer gradual heating model represented with  $(\hat{A}_\Omega, \hat{t}_g, 1)$  in Fig. 3. The FE discretisation is carried out in accordance with characteristic length  $\kappa = \sqrt{\alpha t_h}$  with  $r = 0.8$  mm which leads to a model with only 19, 256 elements. In order to check the mesh convergence, the calculation is repeated using mesh A with 580, 000 elements, as discussed in “Numerical experiments” section and a difference of less than 1% is observed considering the difference between the peak and ambient temperatures for point M.

The temperature evolution using the gradual heating model for points M, D1 and D2 are shown in Figs. 5, 6a, b, respectively. Recall that point D1 is 5 layers below point M and point D2 is 5 layers below D1. It is observed that the gradual heating scheme significantly underestimates the peak temperature for point M located at the top of the deposited layer; see Fig. 5. However, a better agreement between gradual heating and flash heating schemes is observed for far-field temperatures. For point D2 (see Fig. 6b), the difference between peak and ambient temperatures is 14% lower than the reference model. It is also seen that cooling rates of the gradual heating simulations approximate those of flash heating.

Until now, only single layer deposition has been investigated. It remains to analyse the temperature evolution for the deposition of all 20 layers. To ensure computational tractability, only layer-by-layer models are considered for the multi-layer simulations. Fig. 7 shows the temperature variation for point M with  $x_3 = 5.05$  mm as obtained using layer-by-layer flash and gradual heating models. It can be seen from Fig. 7 that the observation made in “Influence of in-plane lumping” section about gradual heating underestimating peak temperatures remains valid only for the first few layers. However, as point M on the first layer becomes increasingly distant from the topmost layer for subsequent layers, the mismatch between the thermal histories significantly reduces. The percentage difference between flash and gradual peak temperatures is calculated for each layer, which is less than 20% after 7th layer. This is emphasised by the closeup view of the thermal history shown for 7–20 layers in Fig. 7. This is simply another example of gradual heating capturing the far-field temperatures. Several examples in the literature show that

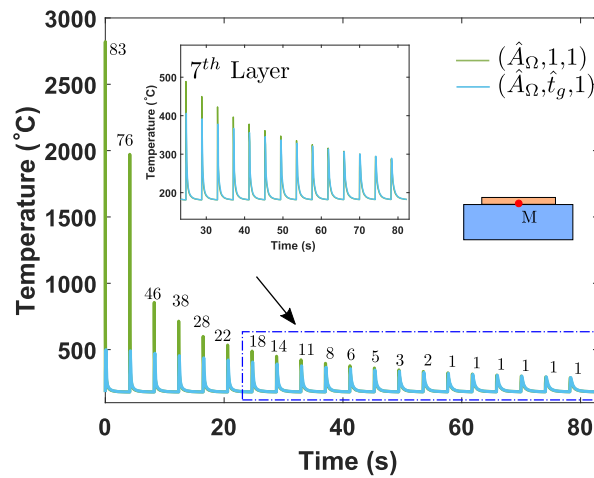


**Fig. 7** Temperature versus time at point M for deposition of all 20 layers in a layer-by-layer manner with flash heating,  $(\hat{A}_\Omega, 1, 1)$  and gradual heating,  $(\hat{A}_\Omega, \hat{t}_g, 1)$ . The percentage difference between temperature peaks using flash and gradual heating are indicated for every layer

gradual heating predictions are validated with thermocouples located at a certain distance from the topmost layer [37, 38, 48]. This is consistent with the findings illustrated in Fig. 7.

Recall that flash and gradual heating schemes represent two extremes to define the heating times. Alternatively, any in between value can also be used. For example, Patil et al. [40] used  $t_h = 1$  ms for layer-by-layer simulation, arguing that the peak values reach the melting point, while higher  $t_h$  values lead to peak temperatures below the melting point. As seen in “Mesh considerations” section, the definition of heating time has a consequential effect on mesh requirements and computational cost. Therefore, the choice of heating time should be carefully made based on the model’s purpose and the desired level of accuracy. While aiming to predict far-field temperatures, gradual heating allows for a coarser mesh, leading to a reduced computational cost. On the other hand, if peak temperatures in the vicinity of the layer being deposited are aimed to be captured, then flash heating is adequate. Another important aspect is the quantitative definition of far field distances i.e. at which distance the temperature values agree well with those found using extended heating times. For example, for the case shown in Fig. 7, the error is less than 20% after the 7th layer. However, the exact determination of this distance depends on various factors such as part geometry, thermal properties and process parameters. Moreover, as evident from Fig. 7, the pragmatic way to determine this length would be based on the desired level of accuracy. Consequently, extending heating times is promising for capturing far-field temperatures in a computationally inexpensive manner, and it has already been used in several studies in the literature. For example, Chiumenti et al. [37] and Neiva et al. [38] compared the thermal histories recorded using thermocouples located at 5.24 mm and 2.5 mm below, respectively, with gradual heating. An excellent agreement was found, which demonstrates the usefulness of this method.

The importance of having a fine temporal resolution to capture far-field temperatures during the cooling phase has already been emphasised in “Mesh considerations” section motivated by the 1D analytical solution detailed in “Appendix”. The effect of time step size on the predicted thermal history is given in Fig. 8. Here, temperature variation for point M using the layer-by-layer flash heating model is calculated using two different time

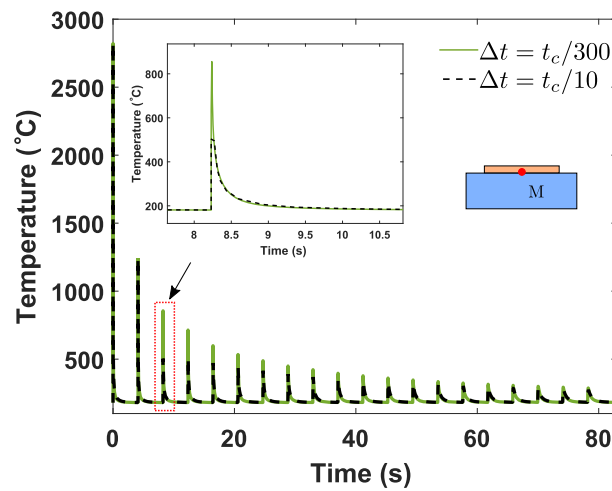


**Fig. 8** Thermal history for deposition of 20 layers using a layer-by-layer flash heating ( $\hat{A}_{\Omega,1,1}$ ) model with two selected time step values. The thermal history is reported for point M located at the top of the first layer

step values during the cooling stage. The green curve shows the temperature evolution with a time step  $t_c/100$  while the dotted black curve presents the same with a time step of  $t_c/10$ . Although the first temperature peaks are identical, far-field peak temperatures are underestimated when  $\Delta t = t_c/10$ . This error is especially pronounced at the beginning of the cooling stage when there is a sharp drop in temperature. This numerical error could lead to erroneous predictions of the thermal history information used to predict, for example, microstructure evolution. Therefore, it is essential to perform a temporal convergence study to obtain accurate temperatures.

#### Influence of out-of-plane lumping

Recall that a volumetric heat source is used for prescribing the heat input in our simulations. Therefore, the energy input per layer should be increased for thicker (lumped) layers, making the lumped layer simulations energy consistent. Also, the cooling time for the out-of-plane lumped layers is adjusted so that the total simulation time remains the same. In this section, we consider point N located on the centre line shown in Fig. 2 at  $x_3 = 5$  mm for comparing the thermal histories.

First, flash heating models with and without lumping are compared. Fig. 9 depicts the thermal history for out-of-plane lumping with  $\hat{l} = 1$  (no out-of-plane lumping)  $\hat{l} = 2$  and  $\hat{l} = 5$ . The closeup view of the first peak is shown as an inset where it is observed that the peak temperatures increase with the number of layers lumped. This is because more energy is deposited during the flash heating time with increased lumping. However, this increment is not linear owing to highly non-linear boundary conditions where the radiation losses increase proportionally to  $T^4$ .

Next, gradual heating for  $\hat{l} = 5$  is considered and the resulting thermal history is shown in Fig. 10. Note that this implies that new layers are subjected to a heating time that is five times longer than that for the flash heating case ( $\hat{A}_{\Omega, 1, 1}$ ) while the heat source value  $\hat{Q}_v'''$  reduces following Eq. (9). As expected, significantly lower peak temperatures are exhibited compared to the case of flash heating. However, for the case of far-field temperature evolution, the lumped gradual model is more accurate than the lumped flash

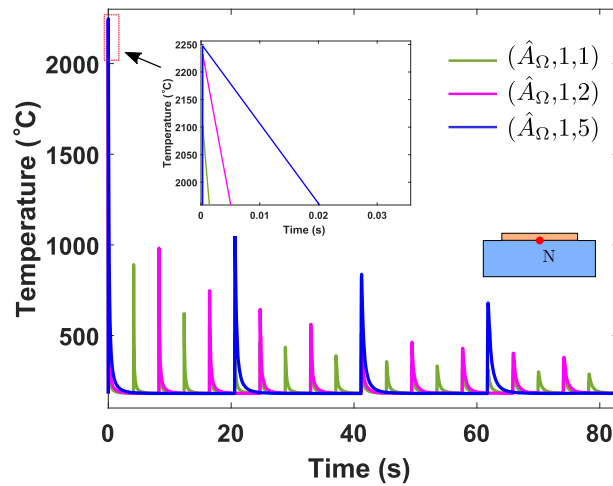


**Fig. 9** Temperature evolution for the entire part considering layer-by-layer flash heating with different degrees of out-of-plane lumping

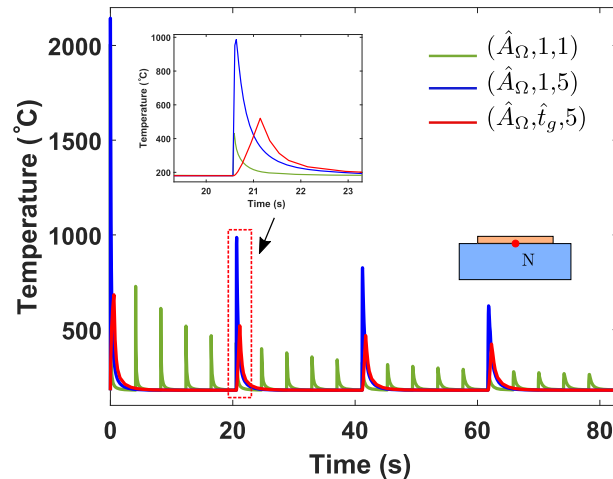


**Fig. 10** Temperature evolution for the entire part considering layer-by-layer flash and gradual heating

heating when compared to the high-fidelity (reference) model with  $(\hat{A}_\Omega, 1, 1)$ . Finally, the FE mesh used for lumped gradual heating models is even more coarse with 456 and 789 elements for lumping of  $\hat{l} = 2$  and  $\hat{l} = 5$ , respectively. Once again, convergence is ensured by checking against mesh A described in “[Mesh considerations](#)” section.

**Discussion**

To gain a deeper perspective on the observations reported in “[Numerical experiments](#)” section, the findings of this paper are compared against the existing literature. For this purpose, a thorough review was conducted on part-scale MAM thermal or thermo-mechanical models. As thermal history acts as an input to mechanical analysis, thermal history directly impacts mechanical predictions. Hence, thermo-mechanical models were also considered in this review. The review includes both PBF and DED process models illustrated in the simplification space presented in Fig. 11. Recall that different normalisation constants are used for different processes (see Table 1). Here, the points with the same colour signify multiple simplified cases considered in the same study. The simplified

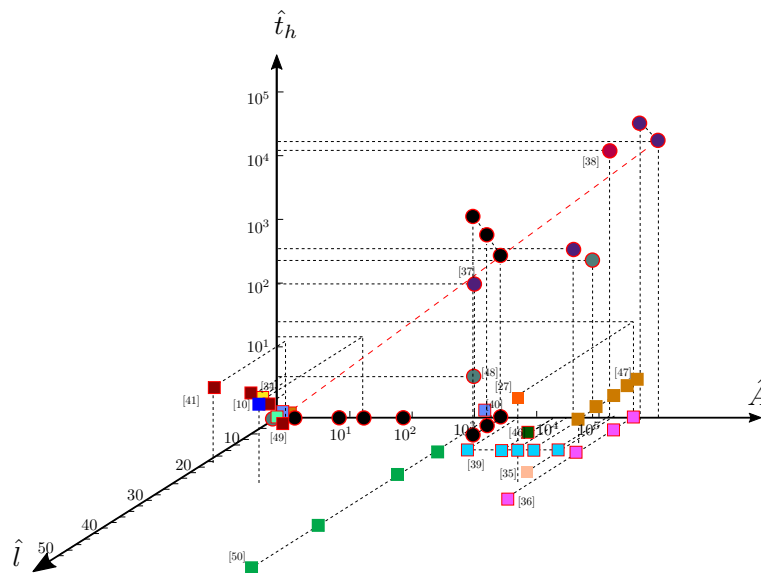


**Fig. 11** Classification of MAM thermal or thermo-mechanical models based on assumed spatial and temporal simplifications. The axes represent the normalised values of in-plane lumping ( $\hat{A}$ ), exposure time ( $\hat{t}_h$ ) and out-of-plane lumping ( $\hat{l}$ ). Note that scales are different for each axis, and the same colours denote different considerations in a single study. Thermal models are marked using circular markers, while thermo-mechanical models are shown with square markers. The models considered in this paper are indicated using black coloured markers. A red boundary around the marker signifies time consistency

thermal models analysed in this paper are indicated in black. Circles are used for thermal models, while squares are used for thermo-mechanical models. A dotted red line on the  $\hat{A}-\hat{t}_h$  plane indicates gradual heating. Recall that the concept of time consistency was introduced in “[Classification of simplifications](#)” section, where cooling time is adjusted in accordance with spatial/temporal simplification. Time consistency is especially important for the case of out-of-plane lumping as larger cooling times compensate for the higher heat capacity of thicker lumped layers [36,41]. The red boundary around the markers in Fig. 11 indicates time consistency, and it is evident that most simplified models in the literature follow this idea. The time consistency condition could not be determined for the markers without a red boundary based on the information provided in the respective papers.

Table 4 summarises the qualitative trends observed in “[Numerical experiments](#)” section in terms of the variation of peak temperatures and far-field temperatures with increasing in-plane lumping or patch size, heating time and out-of-plane lumping. Here, over and under estimation trends are represented by + and – symbols, respectively, while little or no effect of a particular simplification on the predictions is represented by  $\approx$ . Studies with similar findings are also tabulated next to the respective trend. It is apparent from Table 4 that these previous studies already provided insights into the influence of simplifications on the simulation outcomes. However, no single study investigated the entire simplification space. To emphasise this, models from existing literature are further classified based on the phenomena they aim to capture. Figure 12a, b show the simplification space with models discussing the effect of simplifications on peak and far-field temperatures, respectively. This classification highlights how the findings of this study complement existing knowledge. The models from this paper that investigate the influ-



**Table 4** Qualitative trends for each simplification considered for MAM

Simplification	Peak temp.	Far-field temp.
$\hat{A} \uparrow$	$\approx$ [39]	$\approx$
$\hat{t}_h \uparrow$	—	$\approx$ [37,38]
$\hat{l} \uparrow$	+	+ [36,47]

Similar observations from literature are denoted. The symbol of ‘ $\uparrow$ ’ signifies an increase in the degree of simplifications

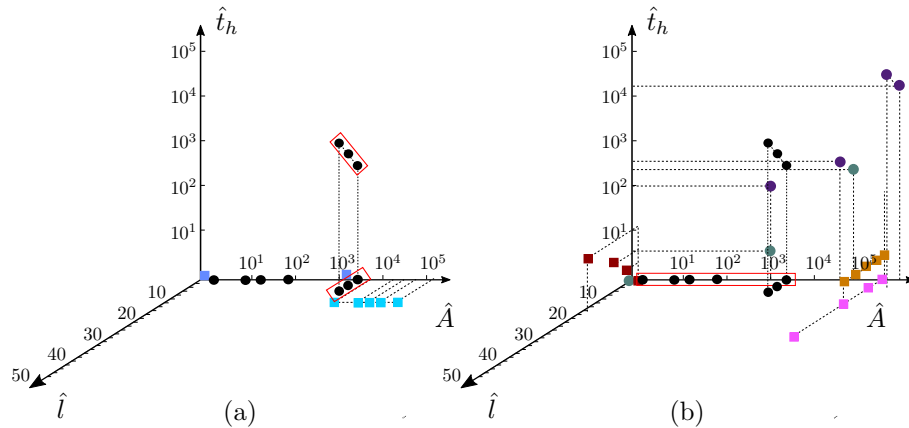


**Fig. 12** The simplification space showing the simplified models which focus on **a** peak and **b** far-field temperatures. Earlier papers that considered more than one point in the simplifications space are shown here. A red box is marked encapsulating the models which investigate the influence of any simplification for the first time

ence of a particular simplification for the first time are enclosed in red boxes in Fig. 12. The influence of out-of-plane lumping and heating times on peak temperatures and the influence of in-plane lumping on far-field temperatures is investigated for the first time here. However, this does not make the other simplified models in this work redundant since a comprehensive investigation of the entire simplification space resulted in an improved understanding of trends that were observed previously. For example, Zhang et al. [36] observed an increase in far-field temperatures with increasing out-of-plane lumping, and constant cooling time was conjectured to be the reason behind this increase. However, as found in this study, the primary reason for this increase is the simultaneous deposition of a larger amount of energy. Moreover, Chiumenti et al. [38], Neiva et al. [37] showed that extended heating times can capture far-field temperatures. However, our analysis complemented this observation with the associated mesh requirements. Moreover, it is shown that the accuracy of far-field temperatures would depend on the distance between the point of interest and the topmost layer.

The wall-clock computational times associated with thermal models with different simplifications are listed in Table 5. All computations were performed using 16 cores on a HPC cluster. It is evident that computational time reduces as the level of simplifications increases. The computational times associated with thermal models are pictorially shown in Fig. 14a where considered models, represented by circles, on the simplification space. The radii of the circles are in the same proportion as the associated computational time. It is important to note that four patch-by-patch models with varying in-plane lumping simulate only deposition of the first layer for computational tractability, while

**Table 5** Computational (wall-clock) time in hours for thermal models presented in this paper

Simplification	Time (h)	Relative (%)	No. of layer(s)	No. of patch(es)
Thermal models				
$(\hat{A}_\Omega/400,1,1)$	317.1	100	1	400
$(\hat{A}_\Omega/256,1,1)$	220.5	69	1	256
$(\hat{A}_\Omega/100,1,1)$	89.1	28	1	100
$(\hat{A}_\Omega/25,1,1)$	20.7	6	1	25
$(\hat{A}_\Omega,1,1)$	55.6	17	20	1
$(\hat{A}_\Omega,\hat{t}_g,1)$	1.1	0.4	20	1
$(\hat{A}_\Omega,1,2)$	39.1	12.7	20	1
$(\hat{A}_\Omega,\hat{t}_g,2)$	1.0	0.3	20	1
$(\hat{A}_\Omega,1,5)$	14.5	4.5	20	1
$(\hat{A}_\Omega,\hat{t}_g,5)$	0.7	0.2	20	1

All computations are performed using 20 cores on a HPC cluster

(lumped) layer-by-layer models simulate deposition of all 20 layers. It can be seen that even with only one layer deposition, the computational cost associated with  $(\hat{A}_\Omega/400,t_f,1)$  is the highest. This shows that the computational burden increases significantly as a flash heating model approaches the origin of the simplification space. Examples of such high-fidelity but computationally burdensome models from the literature are Denlinger et al. [49] and Patil et al. [40]. It is clear from Fig. 14a that significant computational benefits are gained when considering (lumped) layer-by-layer flash heating models compared to models that consider patch-by-patch deposition. However, the maximum computational gains are achieved by gradual heating models with  $(\hat{A}_\Omega,t_g,5)$  requiring only 0.23% of computational time as compared to  $(\hat{A}_\Omega/400,t_f,1)$ . This is mainly because the gradual heating models have much lower spatio-temporal discretisation requirements for numerical convergence. This is evident by the fact that number of elements in model  $(\hat{A}_\Omega,t_g,5)$  is only 1% of  $(\hat{A}_\Omega/400,t_f,1)$ .

In the context of mechanical simulations, there are two effects through which the spatial and temporal simplifications influence the results. First, as discussed previously, the thermal history directly affects the thermal strain, which acts as an input to the mechanical simulation. Second, the spatial simplifications of in-plane and out-of-plane lumping control the mechanical boundary conditions influencing the mechanical field quantities. A brief discussion on both aspects is provided next.

Correct prediction of peak temperatures is crucial for further assessment of stresses and deformations. Based on this, it can be expected that models located on or close to the flash heating plane that correctly capture the peak temperature are appropriate for coupling with mechanical analysis. This is also observed from the existing literature as most reviewed thermo-mechanical models are located on the flash heating plane; see Fig. 11. The models located above the flash heating plane, i.e. in [27,40,47], a slightly higher heating times ensure the melting point has been reached. In fact, in [40,47], attainment of melting point is used as a criterion to decide the value of heating time. Gradual heating models, which lead to under-estimation of peak temperatures are deemed not suitable as an input for the mechanical simulations.

The second effect through which in-plane and out-of-plane lumping simplifications influence the result of the mechanical analysis is through their implications on the

mechanical boundary conditions. For example, Bayat et al. [39] showed that a layer-by-layer model leads to an unrealistic symmetrical stress pattern while a patch-by-patch model where patches emulate laser scanning leads to a more realistic stress development aligned with deposition direction. This is an example of the influence of in-plane lumping on stress directions. Similar observations have been made in the context of out-of-plane lumping as well. Williams et al. [50] showed that accurate predictions can be made until a lumped layer thickness of 0.8 mm i.e.  $\hat{l} = 16$ . However, overestimation was observed for higher lumped layer thickness values. Another study by Zhang et al. [36] investigated the effect of lumping on residual stresses and argued that out-of-plane lumping above  $\hat{l} = 4$  should be avoided. In both these studies, the common finding is that the concept of out-of-plane lumping works up to a certain degree while preserving reasonable accuracy. Note that for a given part, a simulation with a thicker layer implies an artificial reduction in the number of heating-cooling cycles, which also has a direct impact on residual stress development. Moreover, thicker layers have higher stiffness, which are less prone to deformations and lead to an underestimation of deformations. Lastly, other modelling choices such as inclusion of geometrical non-linearity and consideration of powder in the simulation domain can also influence the result of mechanical analysis, as analyzed by Burkhardt et al. [51].

Lastly, it is well known that part geometry also significantly influences the thermal history and it remains to discuss the usability of aforementioned simplified models for the purpose of capturing the influence of geometrical features. It is observed in the existing literature that both flash and gradual heating models can capture the influence of geometry. For example, Hodge et al. [10] utilized a high fidelity moving heat source simulation, located near the origin of the simplification space and increase in the local temperature near an overhanging feature was observed. We note is passing that the computational burden associated with such a model makes it computationally intractable to use it for real size parts. This issue persists for all models located on the flash heating plane due to their fine mesh requirements, as demonstrated in “[Mesh considerations](#)” section. This is also evident by the fact that all studies located on the flash heating plane in Fig. 11 consider only small fully solid cube/cuboidal shapes. Next, the gradual heating models with less strict mesh requirements are also reported to capture the effect of geometry. An example of this is the study by Neiva et al. [38] where a prismatic wedge shape was considered and thermal history predicted by a layer-by-layer gradual heating model was compared with that captured by thermocouple measurements. The findings of Neiva et al. [38] show that gradual heating model was able to accurately capture the geometry induced overheating as elevated temperatures were experienced in the vicinity of an overhanging feature. This indicates that although gradual heating scheme under-predicts local temperature values, it can still be used to qualitatively capture the influence of geometrical features on the temperature response. A similar observation was also reported in our previous work [52], where the temperature history obtained by a lumped layer-by-layer gradual heating model was compared with optical tomography (OT) data recorded while part fabrication. The OT data is a measure of integrated radiation over the period of layer deposition and hence, considered as an indicator of heat accumulation [53]. In order to re-emphasize this comparison between OT data and thermal simulation output, the results are reproduced here in Fig. 13 where the considered part, peak temperatures for each nodal point and spatial OT map are shown in Fig. 13a–c, respectively. It shows that gradual heating with

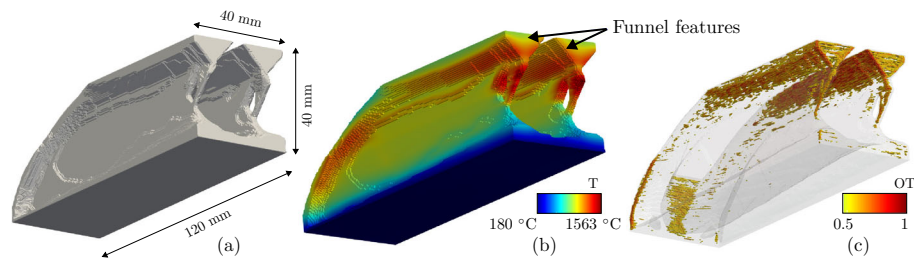


**Fig. 13** **a** A real size AM part analyzed for heat accumulation. **b** Maximum temperature attained for each nodal point as an indicator of overheating. The thermal history is obtained using a layer-by-layer gradual heating model and it shows that gradual heating can qualitatively capture influence of geometric features on thermal history. **c** Visualization of optical tomography (OT) data recorded during part fabrication, the funnel shapes are identified as the cause of heat accumulation where high OT values are seen. These results are reproduced from [52] where further details can be found

super layer thickness of  $500 \mu\text{m}$  i.e.  $\hat{l} = 6.25$  correctly identifies the funnel shaped features which cause overheating, as evident by high OT values. These examples suggest that both flash and gradual heating models would capture the influence of geometry on thermal history. This implies that the general trends observed on the simple cuboidal shape in “Numerical experiments” section will qualitatively remain valid even when considering a complex shape. However, exact quantitative effect will be geometry dependent and will require investigation on a case-by-case basis.

### Recommendations

The trends listed in Table 4 are pictorially shown over the simplification space in Fig. 14. Here, the trends associated with the variation of peak and far-field temperatures with respect to simplifications are shown in Fig. 14b and c, respectively. The size of the circle associated with the reference model closest to the origin represents the reference value (marked with ‘\*’), while over or under prediction associated with a simplified model is represented by the relative size of the circle associated with that model.

These trends assist in making informed choices while setting up a part-scale MAM model. For example, if the aim is to capture the peak temperatures, then flash heating models should be used to provide accurate peak temperature predictions, as evident from Fig. 14b. In literature, peak temperatures have been primarily used for three purposes: identification of problematic geometric features which accumulate heat [9, 10], calculation of cooling rate for microstructural analysis [46] and analysing the influence of scan strategy on residual stresses [54]. For the first two, layer-by-layer flash heating models are appropriately providing an adequate balance between accuracy and computational cost. However, if the purpose is to analyse the effect of the scanning strategy, a patch-by-patch model should be considered. On the other hand, gradual heating models should be avoided as they can lead to significant underestimation while capturing peak temperatures. However, values between flash and gradual heating can be used to find a balance between accuracy and computational cost. For example, as demonstrated by Patil et al. [40],  $t_h = 1 \text{ ms}$ , which is twice the flash heating time leads to peak temperatures around the melting point.

Next, if the aim of the model is to capture far-field temperatures, then gradual heating models should be preferred as they can provide accuracy with significantly less compu-

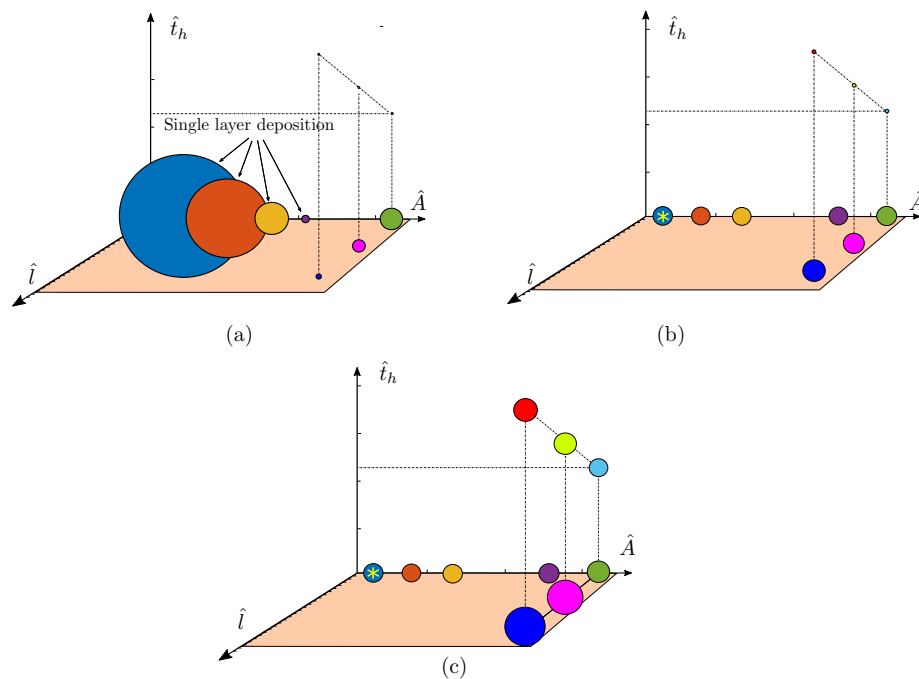


**Fig. 14** The 3D simplification space with the qualitative trend of variations for **a** computational time **b** peak temperatures and **c** far-field temperatures. The circle size shows the trends with radius indicating the relative values of respective parameters as observed in this paper. The reference value marked with '\*' sign is calculated using the reference model

tational effort, as evident from Fig. 14a and c. Moreover, they are found to be useful for capturing influence of geometry and prediction of hotspots. Finally, flash heating models are recommended if the thermal model is used as an input for mechanical analysis. As highlighted in “Discussion” section, correct prediction of peak temperatures is important for mechanical analysis; hence, the earlier recommendations for capturing peak temperatures should be followed. The use of patch-by-patch models is suggested for capturing the directional nature of stresses, as shown in [39], while out-of-plane lumping is recommended for computational tractability. However, determining optimal patch size and out-of-plane lumping factor, which provide an adequate balance between accuracy and computational times, remains a non-trivial task and requires attention on a case-by-case basis. A numerical convergence study for finding these parameters is recommended. Finally, gradual heating models should not be used for this purpose as they significantly underestimate peak temperatures.

## Conclusions

In this paper, the influence of commonly used spatio-temporal simplifications for part-scale modelling of MAM processes has been thoroughly investigated. The two spatial simplifications of in-plane and out-of-plane lumping and one temporal simplification of heating time have been studied. Using numerical models with varying levels of simplifications, it has been found that layer-by-layer models are sufficient for capturing peak temperatures. In contrast, patch-by-patch models are required for analysing the influence of scan vectors. Also, it has been concluded that if peak process temperatures are to be captured, flash heating with no temporal simplification should be used. However, the strict

numerical discretisation requirements associated with flash heating must be carefully ensured. On the other hand, the gradual heating schemes with temporal simplification have been shown to be suitable for capturing far-field temperatures in a computationally efficient manner since they also allow for much coarser spatial numerical discretisation.

No earlier work has holistically characterised the simplifications to the best of our knowledge, where the influence of each simplification has been studied on common MAM attributes. This study provides a broad perspective for choosing/avoiding any particular simplification while developing a MAM model. The work also led to the identification of certain open questions which require attention for further refining the understanding of simplifications. For example, guidelines for quantifying far-field distances could assist in a broader application of gradual heating models. Finding the appropriate lumping factor for in-plane and out-of-plane lumping, which provides an adequate balance between accuracy and computational time, is also an important avenue for future research. In this regard, first, an understanding of part sizes and shapes and their influence on lumping should be developed.

A low volume part with simplified scan pattern was considered in this study as it allowed for utilizing a high fidelity model located near the origin of the simplification space. Typically MAM parts are larger with highly complex geometrical features. Therefore, analysis of a larger more complex part is seen as an immediate future step. In this regard, computational expense associated with high fidelity model of a real-size part is seen as a challenge and specialized computational techniques, e.g. adaptive mesh refinement, might be useful to achieve this goal. Another direct extension of the approach presented in this paper can be the consideration of more simplifications and/or MAM attributes. Here, spatio-temporal simplifications were the primary focus. There are more physics-based simplifications e.g., inclusion/exclusion of convection and/or radiation heat losses and consideration of temperature dependent properties. In this regard, the work by Ranjan et al. [9] analysed the influence of these physics-based simplifications, but only from the context of capturing peak temperatures. Hence, these simplifications can also be characterised using the holistic approach presented in this paper. Additionally, more MAM attributes can be included within the scope of characterising simplifications e.g. cooling rates. Lastly, the framework can also be extended to other AM processes where similar simplifications are commonly used e.g. wire arc additive manufacturing.

### **Appendix: A numerical study using analytical solution for 1D heat transfer**

To capture the temperature transients, adequate mesh resolution is necessary. Therefore, it is crucial to choose the mesh size carefully. A numerical experiment of a simple 1D heat transfer is considered for which the analytical solution is already known to identify the numerical errors.

A one-dimensional domain with length  $L$  is shown in Fig. 15a. The domain is subjected to a heat flux  $Q$  from the top, and the bottom end is assumed to be a heat sink, i.e.  $T = T_0$ .<sup>4</sup> The initial temperature of the domain is also assumed to be  $T_0$ . These boundary and initial conditions are reminiscent of the thermal situation experienced by a typical MAM part.

---

<sup>4</sup>Unlike the 3D case where volumetric heat source was used, here a heat flux boundary condition is defined.

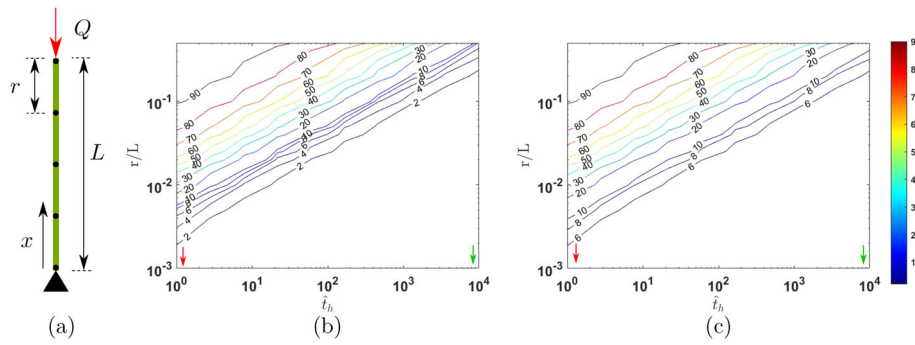


**Fig. 15** **a** 1D domain with length  $L$  subjected to heat flux  $Q$  from top while a heat sink boundary condition is assumed at the bottom. The domain is discretised uniformly using linear elements with length  $r$ . Contour plot of percentage error calculated by comparing analytical and numerical solutions for the peak temperatures obtained at  $x = L$  with **b** time step  $\Delta t = t_h/50$  and **c**  $\Delta t = t_h/5$

The analytical solution representing the evolution of temperature is given as

$$T_h^a(x, t) = T_0 + \frac{Qx}{k} \left[ 1 - 2 \sum_{n=1}^{\infty} \left( \frac{(-1)^{(n+1)}}{\lambda_n^2} \right) \sin \left( \lambda_n \frac{x}{L} \right) e^{-\frac{\lambda_n^2 \alpha t}{L^2}} \right], \tag{10}$$

where  $x$  is position and  $\lambda_n = (2n - 1)\pi/2$ . The detailed derivation is given in [9]. When the heating regime ends, followed by a cooling period, heat flux is removed i.e.  $Q = 0$ . The analytical solution during the cooling period is given as

$$T_c^a(x, t) = T_0 + \frac{2Qx}{k} \sum_{n=1}^{\infty} \frac{(-1)^{(n+1)}}{\lambda_n^2} (1 - e^{-\frac{\lambda_n^2 \alpha t_h}{L^2}}) \sin \left( \lambda_n \frac{x}{L} \right) e^{-\frac{\lambda_n^2 \alpha t}{L^2}}, \tag{11}$$

where  $T_c^a$  represents temperature variation during the cooling regime.

A finite element discretisation scheme is used to solve this boundary value problem numerically. For this purpose, the domain is discretised into linear elements of equal length  $r$  while a time step of  $\Delta t$  is used for the temporal discretisation. An unconditionally stable implicit time integration scheme is used [55]. First, the heating regime is considered and the temperature at the end of the heating step when  $t = t_h$  at  $x = L$  is used for comparing the numerical solution  $T_h^n$  with  $T_h^a$  found using Eq. (10). The numerical experiment is repeated for different normalised heating times and mesh sizes. The percentage error between analytical and numerical solutions is calculated as

$$e = \frac{T_h^a - T_h^n}{T_h^a} \times 100\%. \tag{12}$$

Figure 15b shows the contour levels for the error  $e$  found using different  $r$  values while a constant time step  $\Delta t$  of  $\hat{t}_h/50$  is used. Note that the normalised heating time  $\hat{t}_h$  ranges from the flash heating value (indicated by red arrows) to typical values used in a gradual heating regime (indicated by green arrows).

The first observation from the contour plot reveals that for a fixed level of accuracy, flash heating requires much higher spatial refinement as compared to gradual heating, shown by red and green arrows, respectively. This can be understood by the concept of

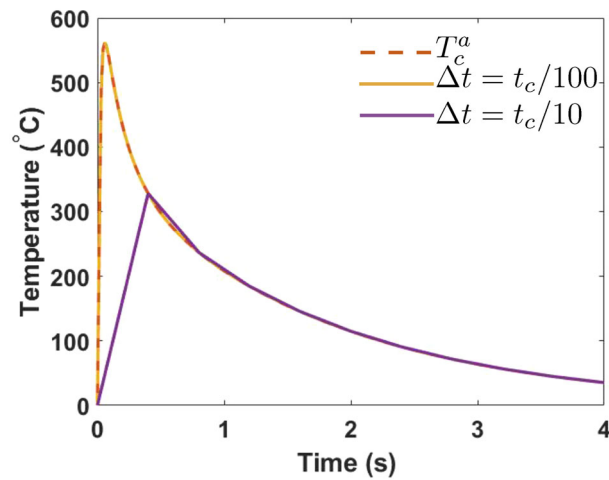


**Fig. 16** The temperature evolution at  $x = L/2$  during the cooling period after a heating step with  $\hat{t}_h = 1$ . The thermal history is found using analytical solution using Eq. (11) and numerically with  $\Delta t = t_c/100$  and  $t_c/10$ , where  $t_c = 4$  is considered

characteristic length given by  $\kappa = \sqrt{\alpha t_h}$ , where  $\alpha$  is the thermal diffusivity. This length signifies the zone of influence near the heat source for short heating times, and a fine spatial resolution is required to capture the steep gradients within this small heat affected zone. Next, time step  $\Delta t = \hat{t}_h/5$  is considered for analysing the influence of time stepping on the accuracy, and the contour plot is shown in Fig. 15c. A slightly higher percentage error is found for the same set of  $r$  and  $\hat{t}_h$ . However, this observation holds only until the percentage error is less than 20%, beyond which the contour plots shown in Fig. 15b and c are virtually identical. This suggests that spatial refinement dictates the solution, and even with very fine temporal discretisation, the correct numerical solution cannot be found unless spatial mesh is refined.

The next observation is associated with the cooling step and far field temperatures. The 1D domain is flash heated for  $\hat{t}_h = 1$  and the evolution of temperature at  $x = L/2$  is found using both analytical solution Eq. (11) and numerical computation. The variation is shown in Fig. 16 where numerical temperature are found using two different  $\Delta t$  values. It is found that the numerical solution with larger time steps leads to under-prediction of far-field peak temperatures. Also, it is observed from the analytical solution that there is a significant variation in temperature during the first few seconds of the cooling step, during which peak value is attained. Therefore, it is recommended to have a fine temporal discretisation, especially at the beginning of the cooling step.

#### Author contributions

Conceptualization: RR, CA, ML and FvK; methodology: RR, CA and ML; software: RR; formal analysis: RR, CA, ML and FvK; writing—original draft preparation: RR; writing—review and editing: RR, CA, ML and FvK; supervision: CA, ML and FvK; funding acquisition: CA, ML and FvK.

#### Funding

This work was performed within PAM<sup>2</sup>, 'Precision Additive Metal Manufacturing', a research project funded by The EU Framework Programme for Research and Innovation—Horizon 2020—Grant Agreement No. 721383.

#### Data Availability Statement

The data used and/or analysed during the current study are available from the corresponding author on reasonable request.



## Declarations

### Competing interests

The authors declare that they have no competing interests.

Received: 9 March 2023 Accepted: 18 October 2023

Published online: 08 November 2023

## References

1. Gibson I, Rosen DW, Stucker B. Additive manufacturing technologies. Berlin: Springer; 2015.
2. Kirchheim A, Dennig HJ, Zumofen L. Why education and training in the field of additive manufacturing is a necessity. 2018. p. 329–36.
3. Kulkarni P, Marsan A, Dutta D. Review of process planning techniques in layered manufacturing. *Rapid Prototyp J*. 2000;6:18–35.
4. Yang Y, Zhou X, Li Q, Ayas C. A computationally efficient thermo-mechanical model for wire arc additive manufacturing. *Addit Manuf*. 2021;46: 102090.
5. Yap CY, Chua CK, Dong ZL, Liu ZH, Zhang DQ, Loh LE, Sing SL. Review of selective laser melting: materials and applications. *Appl Phys Rev*. 2015;2(4): 041101.
6. Parry L, Ashcroft I, Wildman R. Geometrical effects on residual stress in selective laser melting. *Addit Manuf*. 2019;25:166–75.
7. Kolosov S, Boillat E, Gardon R, Fischer P, Locher M. 3D FE simulation for temperature evolution in the selective laser sintering process. *Int J Mach Tools Manuf*. 2004;44(2):117–23.
8. Song B, Zhao X, Li S, Han C, Wei Q, Wen S, Liu J, Shi Y. Differences in microstructure and properties between selective laser melting and traditional manufacturing for fabrication of metal parts: a review. *Front Mech Eng*. 2015;10(2):111–25.
9. Ranjan R, Ayas C, Langelaar M, van Keulen F. Fast detection of heat accumulation in powder bed fusion using computationally efficient thermal models. *Materials*. 2020;13(20):4576.
10. Hodge N, Ferencz R, Solberg J. Implementation of a thermomechanical model for the simulation of selective laser melting. *Comput Mech*. 2014;54:33–51.
11. King W, Anderson AT, Ferencz RM, Hodge NE, Kamath C, Khairallah SA. Overview of modelling and simulation of metal powder bed fusion process at Lawrence Livermore National Laboratory. *Mater Sci Technol*. 2015;31(8):957–68.
12. Schoinochoritis B, Chantzis D, Salonitis K. Simulation of metallic powder bed additive manufacturing processes with the finite element method: a critical review. *Proc Inst Mech Eng Part B J Eng Manuf*. 2015;231:96–117.
13. Zeng K, Pal D, Stucker B. A review of thermal analysis methods in laser sintering and selective laser melting. In: 23rd annual international solid freeform fabrication symposium—an additive manufacturing conference, SFF 2012. 2012. p. 796–814.
14. Yuan P, Gu D. Molten pool behaviour and its physical mechanism during selective laser melting of TiC/AlSi10mg nanocomposites: simulation and experiments. *J Phys D Appl Phys*. 2015;48(3): 035303.
15. King WE, Anderson AT, Ferencz RM, Hodge NE, Kamath C, Khairallah SA, Rubenchik AM. Laser powder bed fusion additive manufacturing of metals; physics, computational, and materials challenges. *Appl Phys Rev*. 2015;2(4): 041304.
16. Rubenchik AM, King WE, Wu SS. Scaling laws for the additive manufacturing. *J Mater Process Technol*. 2018;257:234–43.
17. Khairallah SA, Anderson AT, Rubenchik A, King WE. Laser powder-bed fusion additive manufacturing: physics of complex melt flow and formation mechanisms of pores, spatter, and denudation zones. *Acta Materialia*. 2016;108:36–45.
18. Manvatkar V, De A, Debroy T. Heat transfer and material flow during laser assisted multi-layer additive manufacturing. *J Appl Phys*. 2014;116: 124905.
19. Khairallah SA, Anderson A. Mesoscopic simulation model of selective laser melting of stainless steel powder. *J Mater Process Technol*. 2014;214(11):2627–36.
20. Dai K, Shaw L. Thermal and mechanical finite element modeling of laser forming from metal and ceramic powders. *Acta Materialia*. 2004;52(1):69–80.
21. Roberts IA. Investigation of residual stresses in the laser melting of metal powders in additive layer manufacturing PhD thesis, University of Wolverhampton; 2012.
22. Ly S, Rubenchik AM, Khairallah SA, Guss G, Matthews MJ. Metal vapor micro-jet controls material redistribution in laser powder bed fusion additive manufacturing. *Sci Rep*. 2017;7(1):4085.
23. Bayat M, Mohanty S, Hattel JH. Multiphysics modelling of lack-of-fusion voids formation and evolution in IN718 made by multi-track/multi-layer L-PBF. *Int J Heat Mass Transfer*. 2019;139:95–114.
24. Bayat M, Thanki A, Mohanty S, Witvrouw A, Yang S, Thorborg J, Tiedje NS, Hattel JH. Keyhole-induced porosities in laser-based powder bed fusion (L-PBF) of Ti6Al4v: high-fidelity modelling and experimental validation. *Addit Manuf*. 2019;30: 100835.
25. Bayat M, Nadimpalli VK, Biondani FG, Jafarzadeh S, Thorborg J, Tiedje NS, Bissacco G, Pedersen DB, Hattel JH. On the role of the powder stream on the heat and fluid flow conditions during directed energy deposition of maraging steel-multiphysics modeling and experimental validation. *Addit Manuf*. 2021;43: 102021.
26. Yang Y, Knol M, van Keulen F, Ayas C. A semi-analytical thermal modelling approach for selective laser melting. *Addit Manuf*. 2018;21:284–97.
27. Zaeh MF, Branner G. Investigations on residual stresses and deformations in selective laser melting. *Prod Eng*. 2010;4(1):35–45.
28. Papadakis L, Loizou A, Risse J, Schrage J. Numerical computation of component shape distortion manufactured by selective laser melting (proceedings of the international conference on manufacturing of lightweight components—ManuLight 2014). *Procedia CIRP*. 2014;18:90–5.

29. Peng H, Ghasri-Khouzani M, Gong S, Attardo R, Ostiguy P, Gatrell BA, Budzinski J, Tomonto C, Neidig J, Shankar MR, Billo R, Go DB, Hoelzle D. Fast prediction of thermal distortion in metal powder bed fusion additive manufacturing: part 1, a thermal circuit network model. *Addit Manuf.* 2018;22:852–68.
30. Peng H, Ghasri-Khouzani M, Gong S, Attardo R, Ostiguy P, Rogge RB, Gatrell BA, Budzinski J, Tomonto C, Neidig J, Shankar MR, Billo R, Go DB, Hoelzle D. Fast prediction of thermal distortion in metal powder bed fusion additive manufacturing: part 2, a quasi-static thermo-mechanical model. *Addit Manuf.* 2018;22:869–82.
31. Krol AT, Westhäuser S, Zäh FM, Schilp J, Groth G. Development of a simulation-based process chain–strategy for different levels of detail for the preprocessing definitions. *SNE Simul Notes Eur.* 2011;21:135–40.
32. Keller N, Ploshikhin V. New method for fast predictions of residual stress and distortion of am parts. In: 2014 International solid freeform fabrication symposium 2014. University of Texas at Austin; 2014.
33. Proell SD, Wall WA, Meier C. A simple yet consistent constitutive law and mortar-based layer coupling schemes for thermomechanical macroscale simulations of metal additive manufacturing processes. *Adv Model Simul Eng Sci.* 2021;8(1):24.
34. Lu X, Lin X, Chiumenti M, Cervera M, Hu Y, Ji X, Ma L, Yang H, Huang W. Residual stress and distortion of rectangular and s-shaped Ti-6Al-4v parts by directed energy deposition: modelling and experimental calibration. *Addit Manuf.* 2019;26:166–79.
35. Yu T, Li M, Breaux A, Atri M, Obeidat S, Ma C. Experimental and numerical study on residual stress and geometric distortion in powder bed fusion process. *J Manuf Process.* 2019;46:214–24.
36. Zhang W, Tong M, Harrison NM. Resolution, energy and time dependency on layer scaling in finite element modelling of laser beam powder bed fusion additive manufacturing. *Addit Manuf.* 2019;28:610–20.
37. Chiumenti M, Neiva E, Salsi E, Cervera M, Badia S, Moya J, Chen Z, Lee C, Davies C. Numerical modelling and experimental validation in selective laser melting. *Addit Manuf.* 2017;18:171–85.
38. Neiva E, Chiumenti M, Cervera M, Salsi E, Piscopo G, Badia S, Martín AF, Chen Z, Lee C, Davies C. Numerical modelling of heat transfer and experimental validation in powder-bed fusion with the virtual domain approximation. *Finite Elem Anal Des.* 2020;168: 103343.
39. Bayat M, Klingaa CG, Mohanty S, De Baere D, Thorborg J, Tiedje NS, Hattel JH. Part-scale thermo-mechanical modelling of distortions in laser powder bed fusion–analysis of the sequential flash heating method with experimental validation. *Addit Manuf.* 2020;36: 101508.
40. Patil N, Ganeriwala R, Solberg JM, Hodge NE, Ferencz RM. Benchmark multi-layer simulations for residual stresses and deformation in small additively manufactured metal parts. *Addit Manuf.* 2021;45: 102015.
41. Malmelöv A, Lundbäck A, Lindgren LE. History reduction by lumping for time-efficient simulation of additive manufacturing. *Metals.* 2019;10:58.
42. Manual AU. Abaqus user manual. Abacus; 2020.
43. Rombouts M, Froyen L, Gusarov A, Bentefour EH, Glorieux C. Photopyroelectric measurement of thermal conductivity of metallic powders. *J Appl Phys.* 2004;97:24905.
44. Romano J, Ladani L, Sadowski M. Thermal modeling of laser based additive manufacturing processes within common materials (43rd North American manufacturing research conference, NAMRC 43, 8–12 June 2015, UNC Charlotte, North Carolina, United States). *Procedia Manuf.* 2015;1:238–50.
45. Carslaw HS, Jaeger JC. Conduction of heat in solids. Oxford: Clarendon Press; 1959.
46. Baere DD, Bayat M, Mohanty S, Hattel JH. Part-scale mechanical modelling of LPBF including microstructural evolution effects. In: IOP conference series: materials science and engineering, vol. 861. IOP Publishing; 2020. p. 012013.
47. Kiran A, Hodek J, Vavřík J, Urbánek M, Džugan J. Numerical simulation development and computational optimization for directed energy deposition additive manufacturing process. *Materials.* 2020;13(11):2666.
48. Chiumenti M, Lin X, Cervera M, Wei L, Zheng Y, Huang W. Numerical simulation and experimental calibration of additive manufacturing by blown powder technology. Part I: thermal analysis. *Rapid Prototyp J.* 2017;23:448–63.
49. Denlinger E, Irwin J, Michaleris P. Thermomechanical modeling of additive manufacturing large parts. *J Manuf Sci Eng.* 2014;136: 061007.
50. Williams RJ, Davies CM, Hooper PA. A pragmatic part scale model for residual stress and distortion prediction in powder bed fusion. *Addit Manuf.* 2018;22:416–25.
51. Burkhardt C, Steinmann P, Mergheim J. Thermo-mechanical simulations of powder bed fusion processes: accuracy and efficiency. *Adv Model Simul Eng Sci.* 2022;9(1):18.
52. Ranjan R, Chen Z, Ayas C, Langelaar M, Van Keulen F. Overheating control in additive manufacturing using a 3D topology optimization method and experimental validation. *Addit Manuf.* 2023;61: 103339. <https://doi.org/10.1016/j.addma.2022.103339>.
53. Feng S, Chen Z, Bircher B, Ji Z, Nyborg L, Bigot S. Predicting laser powder bed fusion defects through in-process monitoring data and machine learning. *Mater Des.* 2022;222: 111115. <https://doi.org/10.1016/j.matdes.2022.111115>.
54. Parry L, Ashcroft I, Wildman R. Understanding the effect of laser scan strategy on residual stress in selective laser melting through thermo-mechanical simulation. *Addit Manuf.* 2016;12:1–15.
55. Lewis RW, Morgan K, Thomas H, Seetharamu KN. The finite element method in heat transfer analysis. Wiley; 1996.
56. Prabhakar P, Sames W, Dehoff R, Babu S. Computational modeling of residual stress formation during the electron beam melting process for Inconel 718. *Addit Manuf.* 2015;7:83–91.
57. Mertens R, Clijsters S, Kempen K, Kruth JP. Optimization of scan strategies in selective laser melting of aluminum parts with downfacing areas. *J Manuf Sci Eng.* 2014;136(6): 061012.

## Publisher's Note

Springer Nature remains neutral with regard to jurisdictional claims in published maps and institutional affiliations.